Location and scales of drag reduction in turbulent pipe flow with wall oscillations at low Reynolds number

Daniel J. Coxe, Yulia T. Peet, and Ronald J. Adrian
Arizona State University, School for the Engineering of Matter Technology and Energy, Tempe, Arizona 85281, USA

(Received 21 December 2023; accepted 29 August 2024; published 4 November 2024)

Direct numerical simulations of turbulent pipe flow with transverse wall oscillation and with no transverse wall oscillation are carried out at friction Reynolds numbers $\mathrm{Re}_\tau = 170$, 360, and 720. The period and amplitude of the oscillation are selected to achieve high drag reduction in this low Reynolds number range. The focus of the current study is to identify the location and scales of motion most affected by drag reduction and how they impact drag reduction effectiveness. To answer this question, the streamwise and azimuthal spectra of relevant statistical quantities are analyzed with and without transverse wall oscillation. The effect of wall oscillation is found to suppress the intermediate- and large-scale motions in the buffer layer of the flow, while large-scale motions in the outer layer are enhanced. Since higher Reynolds number flows support development of a growing range of large-scale structures (both in length and height), it is suggested that their prevalence in the energy spectra combined with their negative effect on drag reduction account for a reduced effectiveness of wall oscillation as a drag reduction mechanism with increasing Reynolds number in the actuation regime investigated.

DOI: 10.1103/PhysRevFluids.9.114601

I. INTRODUCTION

Reduction of skin friction drag in turbulent flows is a highly sought outcome of flow control techniques for internal flows. Flow in pipes, with an immediate application to a pipeline transport, is no exception, especially given that 100% of drag comes from skin friction in pipelines due to the absence of other sources of drag [1,2]. Typical friction Reynolds numbers encountered in applications attain the values of $\mathrm{Re}_\tau = 500$–1000 in a long-distance pipeline carrying a light crude oil, due to the high viscosity of crude oil [3]. This is a relatively low range of Reynolds numbers ($\mathrm{Re}_\tau \leqslant 1000$), especially considering that friction Reynolds numbers can reach one to two orders of magnitude higher in applications related to a naval or an aircraft transport [4,5].

A transverse wall oscillation mechanism, wherein pipe or channel walls are oscillated transversely to a mean flow, has been established as a promising drag reduction technique [6–9], which, with some technological advances, can potentially be applied to pipeline applications [10]. Transverse wall oscillation, where the wall velocity changes in time but is kept constant in space, is a special case of a more general drag reduction mechanism via streamwise traveling waves of transverse wall velocity [11–13], which allows for net energy savings. Additionally, it was demonstrated that similar effects of drag reduction can be achieved via spanwise forcing (e.g., with a Lorentz force) [14], and a spanwise rotation [15]. It was recently shown, however, that in channel flows and boundary layers, the effectiveness of these techniques diminishes with increasing Reynolds number [12,13,16–19], even in the low Reynolds number regime ($\mathrm{Re}_\tau \leqslant 1000$) [12,13,17]. The arguments have been proposed explaining drag reduction, and its loss of effectiveness, via a Reynolds-number independence of an upward shift of the mean velocity profile in the logarithmic region of the flow [17,20,21]. On the other hand, it was established that a response of different scales of motions to a

wall oscillation may play a role in this decrease of effectiveness [18,19,22]. The analysis of turbulent scale modification by wall oscillation, however, has not been performed in pipes. Turbulent pipe flow, with an obvious application to a pipeline transport, has some similarities, but also significant differences with channel and boundary layer flows, e.g., in their bulk mean properties [23], spectral characteristics, especially in the large wave numbers [24,25], and in the properties of the Stokes layer of the oscillating wall [26].

The objective of the current study is twofold. First, it aims to establish, via direct numerical simulation (DNS), whether a similar decrease of drag reduction effectiveness with an increase in Reynolds number is observed in pipes with wall oscillation. Second, it intends to investigate the wavelengths, sizes, and locations of eddies that contribute most to drag reduction and interpret this information with respect to established conceptual models of turbulence [27–29]. The knowledge of the affected length scales and their locations in the flow will be useful for analysis and design of improved drag reduction methodologies. It will also be relevant for a development and verification of reduced-order models of drag reduction [30,31].

In this study, three progressively higher Reynolds numbers are considered, $\mathrm{Re}_\tau = 170$, 360, and 720. While DNSs of uncontrolled pipe flows with higher Reynolds numbers have been attempted [32,33], we deliberately restrict ourselves to this relatively low Reynolds number regime for two reasons. First, as mentioned above, this range is applicable to industrial oil pipeline applications. Second, it will allow us to investigate when, where, and why the loss of effectiveness with Reynolds number first originates, at least in the wall oscillation regime considered. In view of this, the current study, rather than attempting to characterize a parametric change in drag reduction across a large range of Reynolds numbers, aims to establish the mechanisms behind the *origin* of a reduced drag reduction effectiveness, focusing on relatively low Reynolds numbers (up to $\mathrm{Re}_\tau = 720$), where small scales of turbulence still dominate over the large scales. We further note that while the number of studies looking at wall oscillation effects in channel and boundary layers at higher Reynolds number flows is steadily growing [18,19,22,34,35], the majority of investigations applied to wall-oscillated pipe flows is still limited to $\mathrm{Re}_\tau \leqslant 170$ (see, e.g., Refs. [36–40]), with the exception of experimental studies by Choi and Graham [8] and by Ding *et al.* [41], where pipe flows up to $\mathrm{Re}_\tau = 962$ and $\mathrm{Re}_\tau = 6000$, respectively, were considered; however, they only provided the drag reduction values, with no evaluation of the structure of turbulence as a result of wall oscillation.

The paper is organized as follows. Section II documents the problem setup and the details of the numerical methodology. Section III summarizes results, including the analysis of a spectral contribution to turbulent kinetic energy, net turbulent force, and bulk mean velocity in pipe flows with and without wall oscillation at three Reynolds numbers, $\mathrm{Re}_\tau = 170$, 360, and 720. Section IV presents conclusions.

II. PROBLEM SETUP

A. Geometry and flow parameters

In this study, a pipe flow with an azimuthally oscillated wall (WO case) is considered as a prototypical configuration to achieve drag reduction, and compared to a standard pipe flow without a wall oscillation (NWO case). The length of the pipe is specified as $L = 24R$, where R is the radius of the pipe (see Fig. 1), following the previous DNS studies of turbulent pipe flows at high Reynolds number [32,42]. The cylindrical coordinate system (x, r, θ) represents streamwise, radial, and azimuthal directions, respectively, with the unit vectors $(\vec{\mathbf{e}}_x, \vec{\mathbf{e}}_r, \vec{\mathbf{e}}_\theta)$ in each direction, and the corresponding velocity vector is $\mathbf{u} = (u_x, u_r, u_\theta)$.

We define the following notations for the globally averaged quantities. Angle brackets without the indices will represent the quantities averaged over streamwise and azimuthal directions, and in time:

$$\langle f \rangle(r) = \langle f(x, \theta, r, t) \rangle_{x,\theta,t}. \tag{1}$$

We define the friction Reynolds number, $\mathrm{Re}_\tau = u_\tau R/\nu$, where $u_\tau = \sqrt{\langle \tau_w \rangle/\rho}$ is the friction velocity, $\langle \tau_w \rangle$ is the mean wall shear stress, ρ is the density, and ν is the kinematic viscosity. The

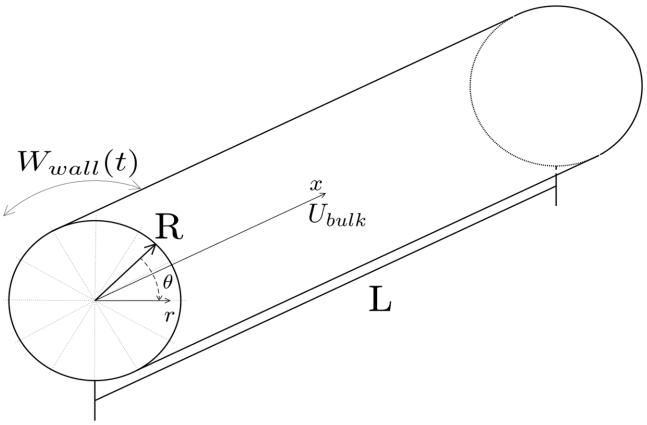

FIG. 1. Cylindrical coordinate system (x, r, θ) represents streamwise, radial, and azimuthal directions, respectively. R is the pipe radius, and L is the pipe length. For the case with no wall oscillation, wall velocity is set to zero: $W_{\text{wall}}(t) = 0$.

bulk Reynolds number is $\text{Re}_{\text{bulk}} = 2\,U_{\text{bulk}}R/\nu$, where U_{bulk} is the bulk mean velocity. This study considers three Reynolds numbers, $\text{Re}_\tau = 170$, 360, and 720, leading to six total cases investigated (two cases—NWO and WO—per Reynolds number).

Viscous wall units are defined by introducing the friction velocity u_τ, the viscous length scale, $l_\tau = \nu/u_\tau$, and the viscous timescale, $t_\tau = \nu/u_\tau^2$. Variables nondimensionalized with these parameters are denoted by superscript $+$. The wall oscillation is achieved by specifying an azimuthal pipe wall velocity as

$$W^+_{\text{wall}}(t) = W_0^+ \sin\left(\frac{2\pi}{T_0^+}t\right), \tag{2}$$

where $W_0^+ = 10$ is the amplitude, and $T_0^+ = 100$ is the period of the wall oscillation, fixed across all three Reynolds numbers. These values are chosen from a set of parametric studies [6–9] that demonstrated high values of drag reduction within this parameter range at Reynolds numbers $\text{Re}_\tau = 200$–500, with the particular values of $\{W_0^+, T_0^+\} = \{10, 100\}$ studied in the works of Choi and Graham [43] and Choi *et al.* [38]. This parameter regime was termed as an "inner-scaled actuation" in some recent studies [34,35], owing to its aim to optimally interfere with the near-wall turbulent cycle.

The governing equations in the current study are the incompressible Navier-Stokes equations:

$$\boldsymbol{\nabla}\cdot\mathbf{u} = 0, \tag{3}$$

$$\frac{\partial\mathbf{u}}{\partial t} + (\mathbf{u}\cdot\boldsymbol{\nabla})\mathbf{u} = -\frac{1}{\rho}\boldsymbol{\nabla}p + \nu\nabla^2\mathbf{u} + \frac{1}{\rho}\mathbf{f}, \tag{4}$$

where $\mathbf{u}$ is the velocity, ν is the kinematic viscosity, ρ is the density, p is the pressure, and $\mathbf{f}$ is the body force. In the current setup, the mean wall shear stress, $\langle\tau_w\rangle$, and hence Re_τ, are fixed between the NWO and WO cases by imposing a streamwise body force, $\mathbf{f} = 2\langle\tau_w\rangle/R\mathbf{e}_x$, which corresponds to a constant mean pressure gradient that balances the wall shear stress [44]. Consequently, the drag reduction which arises as a result of wall oscillation is manifested by an increase in U_{bulk} and a concomitant increase in Re_{bulk}. We can quantify the percent change in bulk mean velocity between the NWO and WO flows as

$$\Delta\,U_{\text{bulk}} = \frac{U_{\text{bulk}_{\text{WO}}} - U_{\text{bulk}_{\text{NWO}}}}{U_{\text{bulk}_{\text{NWO}}}} \times 100\%. \tag{5}$$

TABLE I. Numerical grid parameters for the presented DNS studies. N_{el} denotes the number of elements. Each element contains $(N+1)^3$ collocation GLL points, with $N = 9$ being the polynomial order. N_{gp} is the total number of nonrepeated GLL points within each grid. NWO and WO cases utilize identical grids for each Re_τ. This mesh resolution is comparable with Refs. [42] and [32].

Re_τ	N_{el}	N_{gp}	Δx^+ min/max	Δr^+ min/max	$\Delta(r\theta)^+$ min/max
170	36848	27M	3.5/14.05	0.1/1.6	0.67/2.75
360	238336	173M	2.9/11.90	0.15/2.5	0.81/3.3
720	860160	627M	3.3/13.6	0.22/4.18	1.3/5.4

The skin friction coefficient can be defined as

$$C_f = \frac{2\langle \tau_w \rangle}{\rho\, U_{\mathrm{bulk}}^2}, \tag{6}$$

from which the skin friction drag reduction rate can be calculated as

$$DR = -\frac{C_{f_{\mathrm{WO}}} - C_{f_{\mathrm{NWO}}}}{C_{f_{\mathrm{NWO}}}} \times 100\%. \tag{7}$$

We note that the pressure drag is identically zero in straight pipes (or channels) with smooth walls with and without wall oscillation; therefore, we will refer to the skin friction drag reduction defined in Eq. (7) as "drag reduction". The results presented in Sec. III A will address the Reynolds number dependence of drag reduction in pipe flows with wall oscillation.

B. Numerical methodology

Equations (3) and (4) are numerically solved via DNS using an open-source spectral element solver Nek5000 [45,46]. The spectral element method (SEM) decomposes a computational domain into a collection of elements and utilizes high-order basis functions within each element. In the current implementation, the elementwise basis functions are formed by the tensor product of one-dimensional Lagrange interpolating polynomials of order N associated with the Gauss-Lobatto-Legendre (GLL) quadrature points [45,46].

Numerical grid parameters employed in the current study for the three different Reynolds numbers are listed in Table I. All simulations were executed using ninth-order polynomials as basis functions. Due to a tensor product form of the multidimensional basis functions, the numerical grid in Nek5000 requires hexahedral elements, which are filled with nonuniformly distributed interior GLL collocation points, clustered towards the element boundaries. When reporting resolution in Table I, we indicate the minimum and maximum distances between the collocation points within the element, with the effective (mean) grid spacing lying in between these two numbers. In the radial direction, the elements are clustered towards the wall to achieve 4 gridpoints (not including the wall) below $y^+ = 1$ and 20 gridpoints below $y^+ = 10$. The mean grid spacing of the current DNS is compatible with the DNS guidelines proposed by Pirozolli *et al.* [32]. The temporal integration scheme is an implicit second-order backward difference method for the viscous terms and an explicit second-order extrapolation method for the nonlinear terms. The time step was fixed at $\Delta t = T_{\mathrm{osc}}/8000$ to keep the Courant-Friedrichs-Lewy (CFL) number below 0.75. Periodic boundary conditions were applied in a streamwise direction on both velocity and pressure. No-slip boundary conditions were set up at the pipe wall, with $\mathbf{u}_{\mathrm{wall}}(t) = (u_x, u_r, u_\theta) = 0$ in the NWO case, and $\mathbf{u}_{\mathrm{wall}}(t) = (u_x, u_r, u_\theta) = (0, 0, W_{\mathrm{wall}}(t))$ in the WO case. Validation of Nek5000 as applied to a DNS of turbulent pipe flows with and without wall oscillations can be found in Refs. [39,42,47,48].

For the lowest Reynolds number, $\mathrm{Re}_\tau = 170$, simulations were started from the mean turbulent pipe flow profile approximated by a one-seventh power law [49,50] with superimposed wavelike perturbations [51]. Each subsequent higher Reynolds number case was initialized from a fully

TABLE II. Computational parameters of a postprocessing grid for each Reynolds number. (N_x, N_r, N_θ) correspond to the number of nodes employed in streamwise, radial, and azimuthal directions, respectively; $(\lambda^+_{x\,\mathrm{min}}, \lambda^+_{s\,\mathrm{min,wall}})$ are the minimum streamwise and the minimum azimuthal wavelength at the wall computed by the Fourier analysis.

Re_τ	N_x	N_r	N_θ	$\lambda^+_{x\,\mathrm{min}}$	$\lambda^+_{s\,\mathrm{min,wall}}$
170	384	170	80	21.2	26.8
360	768	360	160	22.6	28.4
720	2048	720	320	15.6	24.4

developed lower Reynolds number case, mapped onto a corresponding finer grid. The WO cases for each Reynolds number were initialized from fully developed NWO cases corresponding to the same Reynolds number. In each case, we allowed for the simulations to reach a statistically steady state (which was monitored through a time series of bulk mean velocity) and subsequently collected statistics for additional $10000t_\tau$. The time to solution for the largest Reynolds number was approximately 800 wall-clock hours using 4096 processors on a KNL partition of the Stampede2 supercomputer at Texas Advanced Computing Center.

C. Postprocessing and notation

For turbulent flows that exhibit a temporal periodicity, the turbulent fluctuations (u_i'') of a random variable are defined to be the deviations of its instantaneous value from its long-time mean $(\langle u_i \rangle)$ plus the periodically varying component of the mean (u_i^ϕ) as [52]

$$u_i = \langle u_i \rangle + u_i^\phi + u_i''. \tag{8}$$

The periodically varying component u_i^ϕ is defined as the phase mean minus the long-time average:

$$u_i^\phi = \langle u_i \mid \phi \rangle - \langle u_i \rangle, \quad \phi = \tau + nT_0, \quad \tau \in [0, T_0),\ n \in \mathbb{N}, \tag{9}$$

with T_0 being the period of oscillation, n an integer number, and the notation $\langle u_i \mid \phi \rangle$ denoting a conditional average given the phase.

Turbulent fluctuations in the current study will be reported as u_i'' for both the WO and NWO cases. Note that for the NWO case, the turbulent fluctuation u_i'' thus defined is equal to a standard turbulent fluctuation as obtained from Reynolds decomposition, $u_i' = u_i - \langle u_i \rangle$, but for the WO case, these quantities are different. Fourier coefficients, spectra, and co-spectra in the streamwise and azimuthal directions are calculated using parallel fast Fourier transform algorithms and presented as functions of wavenumbers (k_x, k_θ), or, equivalently, in terms of the wavelengths, $\lambda_x = 2\pi/k_x$, $\lambda_\theta = 2\pi/k_\theta$. Since the wavelength λ_x has a dimension of length but λ_θ is simply an angular fraction, we also define a dimensional azimuthal wavelength $\lambda_s(r) = r\lambda_\theta$, where r is the local radial location of the variable to be considered.

To perform spectral analysis, the DNS results are transformed from the unstructured SEM grid onto a structured cylindrical grid using Lagrange polynomial interpolation of tenth order (interpolation accuracy of $N + 1$ with $N = 9$ in the current work). The number of nodes (N_x, N_r, N_θ) employed in the postprocessing grid for each Reynolds number is specified in Table II. N_x and N_θ correspond to the number of terms carried in a Fourier analysis, which determines the smallest wavelengths computed as a result of the Fourier analysis as documented in Table II. It can be seen that the smallest computed wavelengths are above the DNS grid resolution, to avoid any spurious oscillations potentially caused by interpolation from the DNS grid and underresolution.

TABLE III. Bulk quantities and their percent change for the WO cases as compared to the NWO cases. In the first three columns, the values in the brackets are presented as (NWO,WO). The percent increase in bulk mean velocity, ΔU_{bulk}, is calculated according to Eq. (5), and the percent drag reduction, DR, as in Eq. (7).

Re_τ	U^+_{bulk}	U_c/U_{bulk}	$C_f \times 10^3$	ΔU_{bulk} (%)	DR (%)
170	(14.4,17.1)	(1.32,1.31)	(9.6,6.8)	18.54	28.8
360	(16.2,18.8)	(1.27,1.25)	(7.6,5.6)	16.25	26.0
720	(18.0,20.5)	(1.26,1.23)	(6.2,4.7)	13.9	22.9

III. RESULTS

A. Drag reduction effectiveness reduces as Reynolds number increases

Table III presents the global quantities for the computed standard (NWO) and drag-reduced (WO) cases, including bulk mean velocity (U_{bulk}), scaled centerline velocity (U_c/U_{bulk}), skin friction coefficient (C_f), and percent change in U_{bulk} and C_f with respect to the corresponding standard (NWO) cases. The current DNS values are in good agreement with previous experimental and computational data, both in terms of the friction factor (four times skin friction coefficient) [42,53–55] and the drag reduction values. In particular, computed drag reduction rates [DR; see Eq. (7)] are comparable with the reported values of 29.9% for channel flow at $\text{Re}_\tau = 200$ (DNS [38]), 34.9% for pipe flow at $\text{Re}_\tau = 150$ (DNS [38]), and 23.0% for pipe flow at $\text{Re}_\tau = 650$ (experiments [8]) for the same values of wall oscillation parameters $\{W_0^+, T_0^+\} = \{10, 100\}$. We remark that at the lowest Reynolds number, the flow is at the onset of transition, and the outcome of drag reduction, especially whether the flow relaminarizes or not [36–38], may be sensitive to the details of the setup (constant flow rate versus constant pressure gradient) and numerical method (the amount of numerical dissipation in the code). From Table III, it is evident that the mechanism of drag reduction with transverse wall oscillations becomes less effective as Reynolds number increases when targeting inner scale actuation. Using a power-law fit, we find that our data obey the relation $DR \sim \text{Re}_\tau^{-\gamma}$, with $\gamma = 0.16$. The value of the coefficient γ is within the range of the previously reported values of γ in channels being anywhere between 0.1 and 0.4, depending on the actuation parameters [12,13,16,17,56]. The current value of $\gamma = 0.16$ is slightly lower as compared to $\gamma = 0.2$ for a channel with the wall oscillation at similar parameter values [12,16,56]. Although within the range of uncertainty, this discrepancy may also exemplify the differences between pipe and channel flows.

It is generally accepted that drag reduction with transversely oscillated walls occurs due to an interaction of turbulence with the so-called Stokes layer [37], which refers to a layer of nonzero phase mean transverse velocity developed over an oscillating wall. For the current frequency of wall oscillation, it can be shown that the Stokes layer thickness over a cylindrical pipe wall is equal to the one obtained in a classical Stokes second problem. Here, we define the Stokes layer thickness as the wall-normal location at which the amplitude of the azimuthal velocity reaches 1% of its wall value, $\delta_{Sl} = 4.6\sqrt{T_0\,\nu/\pi}$ [44]. In wall units, this quantity is equal to $\delta^+_{Sl} = 4.6\sqrt{T_0^+/\pi} \approx 25$ for the chosen $T_0^+ = 100$ across all three Reynolds numbers [26]. Note that this definition is different from the Stokes penetration depth, $\delta^+_{Sp} = \sqrt{T_0^+/\pi}$ [57], and the Stokes layer phase-matching thickness, $\delta^+_{Sm} = \sqrt{4\,\pi\,T_0^+}$ [37,58].

In describing turbulent statistics, we will be referring to different regions commonly identified within the turbulent boundary layer [44,50], in addition to the Stokes layer, as summarized in Table IV, where we use the notation $y^+ = y/l_\tau$, with $y = R - r$. We will be using the asterisk to denote the quantities scaled with the outer dimension, such that $r^\star = r/R$ and $y^\star = 1 - r/R$.

B. Effect of Reynolds number on single point statistics

Figure 2(a) documents the change in the mean velocity as a result of transverse wall oscillation for the three Reynolds numbers. The change is defined as $\Delta f = f(\text{WO}) - f(\text{NWO})$, i.e., the

TABLE IV. Regions within the turbulent boundary layer, including the Stokes layer, referred to throughout this work. The inner layer is the composite of the viscous, buffer, and logarithmic layers while the outer layer is the composite of the logarithmic layer and the wake region of the flow [44,50].

Region	Range
Viscous layer	$y^+ \leqslant 5$
Buffer layer	$5 < y^+ \leqslant 30$
Stokes layer	$y^+ \leqslant 25$
Log layer	$30 < y^+ \leqslant 0.2\mathrm{Re}_\tau$
Wake region	$y^+ > 0.2\mathrm{Re}_\tau$

quantity evaluated with transverse wall oscillation minus the quantity evaluated with no wall oscillation. This convention will be maintained throughout the remainder of the work. For all three Reynolds numbers the maximum change in mean velocity occurs around $y^+ \approx 100$. This location happens to be in the top half of the logarithmic layer for the highest Reynolds number, above the logarithmic layer for $\mathrm{Re}_\tau = 360$, and approaching the centerline of the pipe for $\mathrm{Re}_\tau = 170$. As the Reynolds number increases, the peak change in the mean streamwise velocity reduces. It has been proposed that the drag reduction scales with the upward vertical shift of the mean velocity profile in

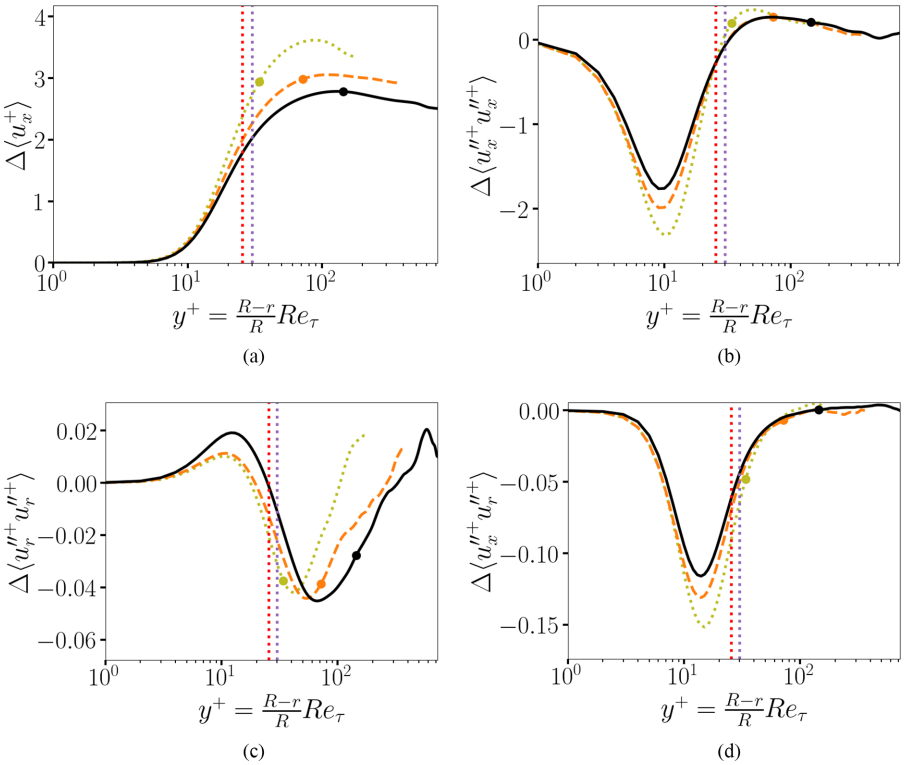

FIG. 2. Change in the mean single point statistics of the flow. Olive green dotted line, $\mathrm{Re}_\tau = 170$; orange dashed line, $\mathrm{Re}_\tau = 360$; black solid line, $\mathrm{Re}_\tau = 720$. Circles indicate the location of the top of the logarithmic layer (Table IV). The vertical red dotted line indicates the top of the Stokes layer; the vertical purple dotted line is the top of the buffer layer. (a) Mean velocity, (b) Streamwise fluctuations, (c) Radial fluctuations and (d) Shear stress.

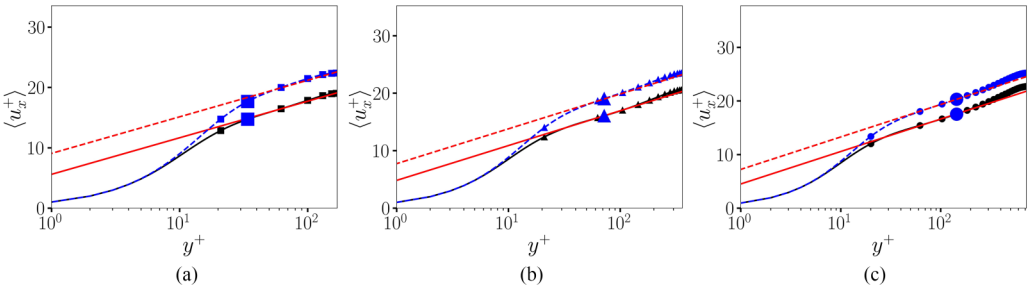

FIG. 3. Mean streamwise velociy profiles in logarithmic scale for (a) $\mathrm{Re}_\tau = 170$, (b) $\mathrm{Re}_\tau = 360$, and (c) $\mathrm{Re}_\tau = 720$. Black lines are NWO, and blue lines are WO. Red lines correspond to the least squares fit of the logarithmic law used to determine the shift, $\Delta B = \Delta \langle u_x^+ \rangle$. The location of the enlarged blue markers indicates the top of the logarithmic layer with respect to each Reynolds number.

the logarithmic region of the flow [17,20,21]. Figure 3 plots the mean velocity profile in logarithmic scale for the WO and NWO flows for the three Reynolds numbers. Considering the logarithmic law of the wall,

$$\langle u_x^+ \rangle = \frac{1}{k} \ln y^+ + B, \tag{10}$$

the log-law shift, ΔB, can be measured directly from the shift in the $\langle u_x^+ \rangle$ plots and is documented in Table V. On the other hand, Gatti and Quadrio [17] proposed the following relationship for ΔB for the constant pressure gradient flows (assuming that the log-law shift does not depend on Reynolds number but only on the drag reduction rate):

$$\Delta B = \sqrt{\frac{2}{C_{f_{\mathrm{NWO}}}}}[(1 - DR)^{-1/2} - 1], \tag{11}$$

where $C_{f_{\mathrm{NWO}}}$ is the skin friction in the uncontrolled case, and DR [see Eq. (7)] is the drag reduction rate. The values of ΔB calculated from Eq. (11) are also presented in Table V for comparison.

Consistent with the observations of Hurst *et al.* [13], the measured shift decreases with Re_τ, but the amount of decrease is diminishing. Gatti and Quadrio [17] argue that the shift becomes independent from the Reynolds number once the latter reaches a high enough value, and the observed trend supports this argument. Futhermore, consistent with the analysis of Yao *et al.* [18], the measured and estimated ΔB values agree well at higher Reynolds numbers ($\mathrm{Re}_\tau = 360$, 720) but deviate more significantly for the lowest one ($\mathrm{Re}_\tau = 170$). This is, again, consistent with the fact that the estimate (11) is only supposed to hold for high enough Reynolds numbers, when the overlap region is well developed [17,18].

Figures 2(b)–2(d) subsequently document the change in the second-order statistics as a result of the transverse wall oscillation. Wall oscillations suppress the streamwise turbulent kinetic energy within the buffer layer for all three Reynolds numbers. Above the buffer layer, streamwise turbulent

TABLE V. The values of the log-law shift, ΔB, as measured from the velocity profile plots in Fig. 3 (second column), and estimated from Eq. (11) by Gatti and Quadrio [17] (third column).

Re_τ	ΔB_{mes}	ΔB_{est}
170	3.4	2.7
360	2.5	2.6
720	2.3	2.5

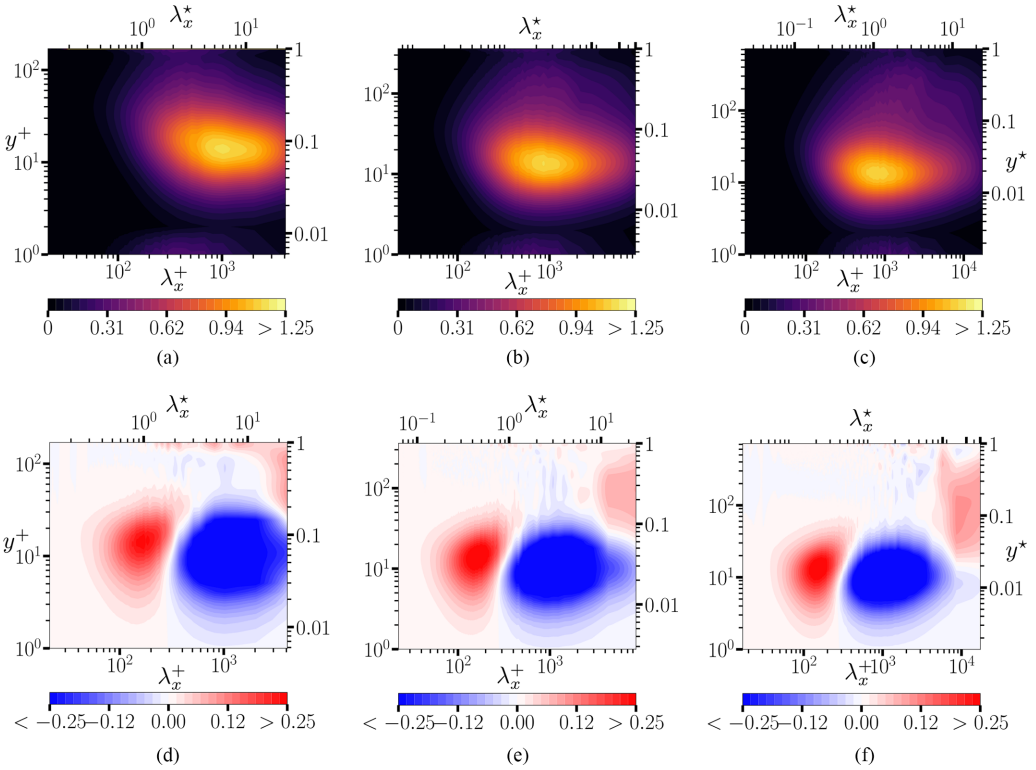

FIG. 4. Premultiplied streamwise kinetic energy as a function of wall-normal location and streamwise wavelength, $k_x\Phi_{u_xu_x}(\lambda_x^+, y^+)/u_\tau^2$: [(a)–(c)] reference spectra (NWO); [(d)–(f)] change in spectra, $k_x\Delta\Phi_{u_xu_x}(\lambda_x^+, y^+)/u_\tau^2$. From left to right: [(a), (d)] $\mathrm{Re}_\tau = 170$, [(b), (e)] $\mathrm{Re}_\tau = 360$, and [(c), (f)] $\mathrm{Re}_\tau = 720$. Axes in the figures scale with viscous units, whose bounds differ across Reynolds numbers.

kinetic energy is slightly increased. Radial turbulent kinetic energy changes are two orders of magnitude smaller than the changes in the streamwise turbulent kinetic energy. Its trends in the buffer and the logarithmic layer are the reverse of those of the streamwise turbulence kinetic energy. The change in the Reynolds shear stress is one order of magnitude smaller than the change in the streamwise kinetic energy. The result of wall oscillations is to suppress the Reynolds shear stress through the top of the logarithmic layer for all three Reynolds numbers.

C. Scale analysis of the drag reduction

1. Turbulent kinetic energy

Figure 4 documents the premultiplied streamwise spectra of the streamwise kinetic energy in the NWO and WO cases, as well as its change, as a result of wall oscillation. It is instructive to interpret the results of the current spectral analysis in relation to a well-established paradigm of hairpin vortices and hairpin vortex packets [28,59] in a turbulent flow. There is a body of literature confirming the existence of such structures within the range of Reynolds numbers presented in the current analysis [60–63]. According to a hairpin model [28,60]: (1) quasistreamwise vortices that are formed in the buffer layer are correlated with the hairpin legs; (2) hairpins have the wavelength $\lambda^+ \sim O(10^2)$ and reside in the buffer and/or logarithmic layer; and (3) hairpin packets have the wavelength $\lambda^+ \sim O(10^3)$ and reside in the logarithmic layer. Figure 4 shows that wall oscillations suppress the energy of the streamwise structures in the buffer layer having wavelengths in the range $300 \leqslant \lambda_x^+ \leqslant 10\,000$. These intermediate- to large-scale structures in the buffer layer correspond

to the concatenation of hairpins and their packets [28,59], whose legs produce a signature of the well-known streamwise streaks in the boundary layer [64]. The energy in the wavelengths of $\lambda_x^+ \leqslant 300$ in the buffer layer is enhanced; however, this effect is exaggerated in a plot of a premultiplied spectra—the amplification is indeed quite subtle if plotted without premultiplication (not shown here for brevity). The enhancement of energy in small scales can be due to a breakdown of streaks into smaller structures as previously observed in wall-oscillated [65] and wall-rotated [15] pipe flows. Another important observation is the enhancement of energy in large streamwise wavelengths $\lambda_x^+ > 5000$ in and above the logarithmic layer of the flow. This amplification of large outer scales in drag-reduced flows has also been observed with other drag reduction mechanisms [66–68] and is hypothesized to be related to a reduction in large-scale bursts that can otherwise disrupt the outer-layer structures [69]. It is worth noting that at the low Reynolds number ($\mathrm{Re}_\tau = 170$) and moderately low Reynolds number ($\mathrm{Re}_\tau = 360$), these large outer-layer structures are restricted by the vertical height of the container and their enhancement is less consequential. The chosen domain size ($L = 24\,R$) is sufficient to capture the large-scale and the very-large-scale motions [32,42], which are known to have lengths of $\sim$(2–3)R and $\sim$(8–16)R, respectively, in uncontrolled flows [70]. Additionally, Coxe *et al.* [71] demonstrated a full decay of the autocorrelation function between streamwise velocity fluctuations over the domain length in both NWO and WO flows. However, Fig. 4 seems to indicate that the differences are observed in large scales of motion throughout the entire domain length. It is important to point out that, while the energy in large scales decays past a certain value, as commensurate with the previous studies [18,24,70], the difference does not necessarily decay, due to a modulation of these scales by wall oscillation. The observed differences, however, are about an order of magnitude smaller than the energy itself.

While scaling of turbulent quantities in plus units (as is done in the current paper) is typical in the analysis of wall turbulence [25], to evaluate the effect of the increased bulk mean velocity (therefore, total mean flow energy) in a drag-reduced flow in the current setup on the results of the current analysis, Fig. 5 presents a comparison of the premultiplied streamwise kinetic energy spectra at selected y^+ locations when normalized in the inner units (with u_τ^2, default normalization) and in the outer units (with U_{bulk}^2) for $\mathrm{Re}_\tau = 720$. It can be seen that, when normalized with U_{bulk}^2, the attenuation of small and intermediate scales of motions in a drag-reduced flow is even more pronounced. However, the increase in energy in the large scales of motion in and above the logarithmic layer is still evident, testifying that this increase is a feature of a turbulence modification and not a consequence of the increased mean energy in the flow.

Wall oscillations also impact the azimuthal energy spectrum of streamwise velocity across the Reynolds numbers (see Fig. 6). The energy in the azimuthal wavelengths associated with the near-wall streak spacing, $\lambda_s^+ \approx 100$–200, is reduced in the buffer layer ($5 \leqslant y^+ \leqslant 30$). Since streaks and quasistreamwise vortices are closely related, wall oscillation presumably weakens the quasistreamwise near-wall vortices, thereby reducing their transport of streamwise momentum into the streaks. As with the streamwise spectrum, the amplification of energy in large azimuthal scales of motion ($\lambda_s \geqslant 1000$) is notable.

2. Net turbulent force

The net turbulent force per unit mass in the axial direction (henceforth referred to as the "net turbulent force") in a turbulent pipe flow is defined as

$$F_{\mathrm{turb}}(r) = -\frac{1}{r}\frac{d\{r\langle u_x'' u_r''\rangle\}}{dr}. \tag{12}$$

It arises from the momentum balance obtained via averaging the streamwise momentum equation along the homogeneous (streamwise and azimuthal directions) and in time as [70,72,73]

$$\left\langle \frac{\partial u_x}{\partial t} \right\rangle = -\frac{1}{r}\frac{d\{r\langle u_x'' u_r''\rangle\}}{dr} + \frac{\nu}{r}\frac{d}{dr}\left(r\frac{d}{dr}\right)\langle u_x\rangle + \frac{1}{\rho}\langle f_x\rangle \tag{13}$$

and has units of acceleration.

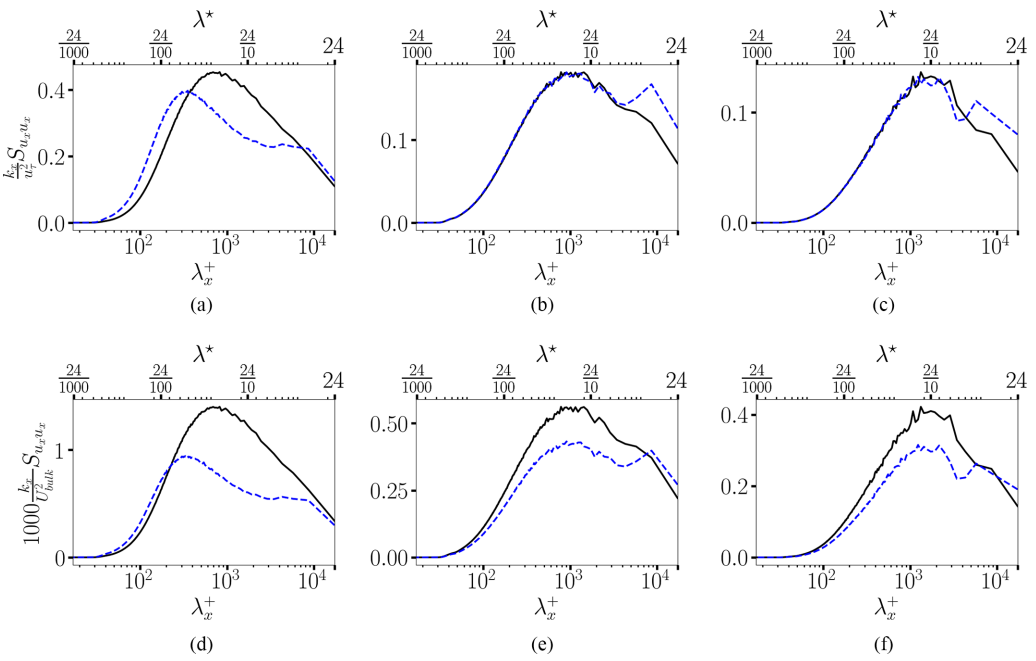

FIG. 5. Premultiplied streamwise kinetic energy spectra normalized with inner units (u_τ^2, top row) and outer units (U_{bulk}^2, bottom row) at selected wall-normal locations of [(a), (d)] $y^+ = 20$, [(b), (e)] $y+ = 100$, and [(c), (f)] $y^+ = 300$ for $\text{Re}_\tau = 720$. Black solid lines are for NWO cases, and blue dashed lines are for WO cases.

The net turbulent force determines the mean local acceleration or deceleration of the mean flow due to the mean turbulent shear stresses. We find that the net mean turbulent force is a more useful measure of the effect of turbulence than the Reynolds stresses. First, it is a vector, not a tensor. Second, it succinctly describes all of the effects of turbulent Reynolds stresses on the mean flow. Third, force is a more intuitive variable to interpret. For example, in steady pipe flow the net mean force balances the contributions from the mean pressure gradient ($-\langle f_x \rangle$) and the viscous stress. At the location of the maximum mean Reynolds shear stress, where one might, at first blush, think that the turbulence has the greatest effect on the mean flow, the net turbulent force is actually zero, indicating no effect of turbulence at all at this value of y. Below the maximum Reynolds shear stress the net mean turbulent force is positive, implying the mean turbulent flow is accelerated above the corresponding laminar profile, thereby increasing the mean wall shear stress. Above the location of the maximum mean Reynolds shear stress, the net mean turbulent force retards the flow compared to the laminar parabolic profile, thereby reducing bulk flow velocity. All these observations rest upon the empirically observed mean shear stress profile.

Utilizing Parseval's theorem, the net turbulent force can be decomposed into a sum of contributions from the streamwise and azimuthal Fourier modes as

$$F^+_{\text{turb}}(r^+) = -\sum_{k_x}\sum_{k_\theta} \frac{1}{r^+} \frac{\partial\{r^+ \, \Phi_{u_x u_r}(k_x, r^+, k_\theta)\}}{\partial r^+}, \tag{14}$$

rescaled in wall units. Figure 7 shows the streamwise spectrum of the net turbulent force, $F^+_{\text{turb}}(\lambda_x^+, y^+)$, as a function of the wall-normal coordinate and the streamwise wavelength for the NWO and WO cases at $\text{Re}_\tau = 720$. We remark that Fig. 7 agrees with the data presented by Wu *et al.* [73] (see their Fig. 17) for the NWO pipe flow if replotted on a log-log scale (not shown here for the sake of brevity). Consistent with previous observations [70,72,73], we find that the net

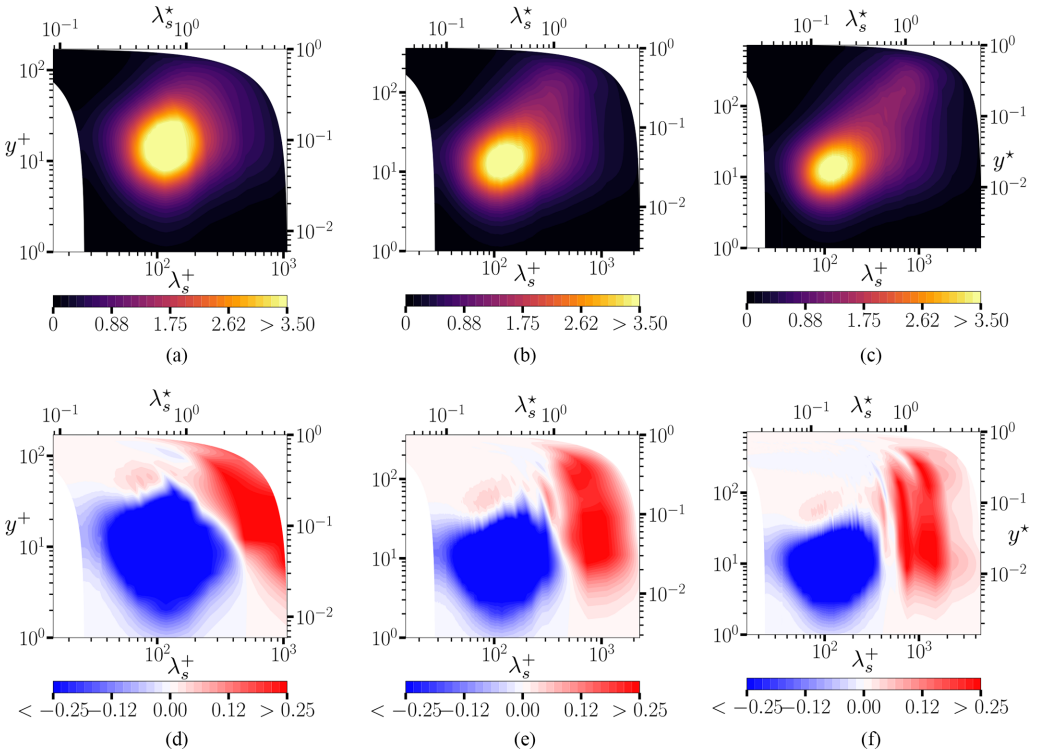

FIG. 6. Premultiplied streamwise kinetic energy as a function of wall-normal location and azimuthal wavelength, $k_\theta \Phi_{u_x u_x}(\lambda_s^+, y^+)/u_\tau^2$: [(a)–(c)] reference spectra (NWO); [(d)–(f)] change in spectra, $k_\theta \Delta\Phi_{u_x u_x}(\lambda_s^+, y^+)/u_\tau^2$. From left to right: [(a), (d)] $\mathrm{Re}_\tau = 170$, [(b), (e)] $\mathrm{Re}_\tau = 360$, and [(c), (f)] $\mathrm{Re}_\tau = 720$. Axes in the figure scale with viscous units, whose bounds differ across Reynolds numbers.

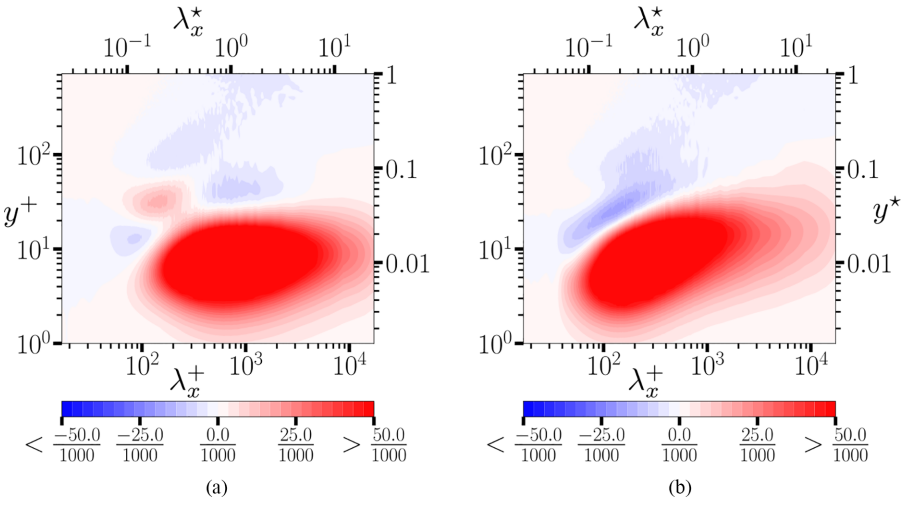

FIG. 7. Premultiplied streamwise spectra of the net turbulent force, $F^+_{\mathrm{turb}}(\lambda_x^+, y^+)$, for $\mathrm{Re}_\tau = 720$. (a) NWO cases; (b) WO cases.

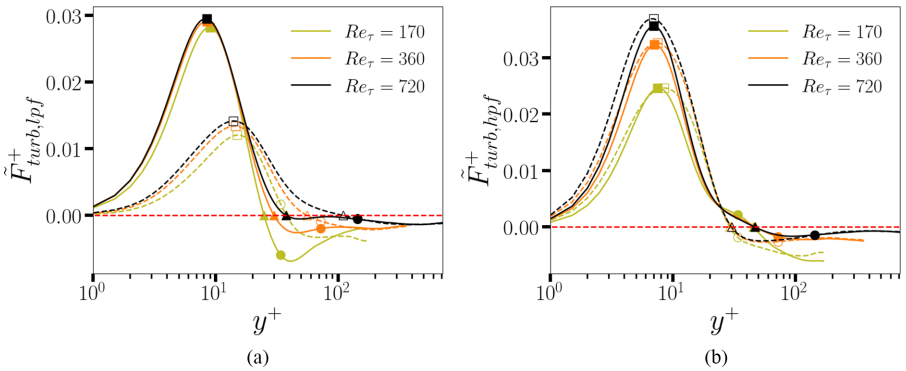

FIG. 8. Filtered net turbulent force profile: (a) low-pass and (b) high-pass filtered net turbulent fore. Squares indicate the location of the maximum net turbulent force, triangles indicate the location of the zero net turbulent force, and circles indicate the top of the logarithmic layer as referenced in Table IV. Solid lines correspond to NWO cases, and dashed lines correspond to WO cases.

force is positive across all the scales of motion $\lambda_x^+ \geqslant 100$ in the buffer layer ($y^+ < 20$), amounting to an acceleration of the mean flow from the corresponding laminar profile, and negative above it, implying retardation. While the net turbulent force affects all scales of motion, the effect is larger for large scales at all Reynolds numbers, consistent with the works of Refs. [70,73]. The impact of the wall oscillations is to reduce this effect, diminishing both the acceleration of turbulent structures near the wall and their deceleration in the outer layer. In general these changes are conducive to drag reduction, since they keep the mean velocity profile closer to its laminar shape.

To separate the effects of large and small scales of motion on the net turbulent force, we apply a Gaussian low-pass filter [59,70],

$$\hat{g}_{lpf}(k_x) = \exp\left(-\frac{k_x^2}{2\sigma^2}\right), \tag{15}$$

with σ being the filter width, and k_x the streamwise wavenumber. We set the filter width such that the strength of the filter is at 50% of its peak at a filter cutoff location, $k_{x,\text{cutoff}} = 2\pi/\lambda_{x,\text{cutoff}}$. This gives the value of $\sigma^2 = k_{x,\text{cutoff}}^2/(2\ln 2)$. The filter cutoff wavelength $\lambda_{x,\text{cutoff}}^+ = 1000$ is chosen to separate the large and very large scales of motion from the small and intermediate scales [59,72]: the scales smaller than the cutoff wavelength are attenuated by the low-pass filter. Conversely, its high-pass-filter counterpart, $\hat{g}_{hpf}(k_x) = 1 - \hat{g}_{lpf}(k_x)$, attenuates the scales with $\lambda_x^+ \geqslant \lambda_{x,\text{cutoff}}^+$. We apply both filters to the net turbulent force spectra. The filtered net turbulent force is defined as

$$\tilde{F}^+_{\text{turb},\{lpf,hpf\}}(r^+) = -\sum_{k_x}\sum_{k_\theta}\frac{1}{r^+}\frac{\partial\left\{r^+\Phi_{u_x u_r}(k_x, r, k_\theta)\right\}}{\partial r^+}\hat{g}_{\{lpf,hpf\}}(k_x). \tag{16}$$

The cumulative low-pass and high-pass filtered contributions are documented in Fig. 8. Additionally, Table VI records the position of the zero net turbulent force for the total (unfiltered) and filtered quantities for the NWO and WO cases, together with the difference between the NWO and WO locations (Δ). We refer to the location of the zero net turbulent force based on the total (unfiltered) quantities as y_{f0}^+.

Figure 8 shows that the wall oscillations significantly attenuate the magnitude of the low-pass filtered net turbulent force while leaving its high-pass filtered counterpart relatively unchanged; i.e., the major effect of the net turbulent force modification is coming from relatively large scales of motion ($\lambda_x^+ > 1000$). A considerable net force reduction in large scales (low-pass filtered contribution) is found all the way from the wall and throughout the top of the logarithmic layer of the flow. Another important effect is the shift of both the maximum and the zero net force locations upwards

TABLE VI. Wall-normal location of the zero net turbulent force in plus units for (NWO,WO) based on unfiltered, low-pass filtered, and high-pass filtered quantities, along with the difference between the WO and NWO locations (Δ = WO−NWO).

Re_τ	(NWO, WO, Δ) unfiltered	(NWO, WO, Δ) low-pass filtered	(NWO, WO, Δ) high-pass filtered
170	(25.8, 31.1,5.3)	(24.9, 38.0, 13.1)	(45.3, 29.2, −16.1)
360	(31.7, 37.1,5.4)	(30.1, 55.9, 25.8)	(47.4, 29.9, −17.5)
720	(39.1, 44.8,5.7)	(37.7, 110.1, 72.4)	(46.7, 30.2, −16.5)

by wall oscillations, which is primarily seen in its low-pass filtered contribution. As can be judged from Table VI, the major effect on the shift indeed comes from the large scales of motion, with the small and intermediate scales (high-pass filtered) contributing less than 20% of the total shift. The small and intermediate scales, shown in Fig. 8(b), promote a slightly higher acceleration of the mean velocity profile near the wall and a slightly higher deceleration between the top of the buffer layer and the top of the logarithmic layer in the WO case, the effect opposite to that of the large scales. Above the logarithmic layer of the flow, large-scale net turbulent force is enhanced in the WO case for the two highest Reynolds numbers, which is contrary to its reduction by the large scales in the inner layer. This is consistent with a reduction of the normalized centerline velocity U_c/U_{bulk}, despite the growth of the bulk mean velocity U_{bulk} in the WO as compared to the NWO cases observed in Table III across all Reynolds numbers: increased (negative) turbulent force in this region acts to decelerate the large-scale structures more significantly in the center of the pipe flow with wall oscillation. This effect indicates a decreased effectiveness of the drag reduction mechanism in the outer layer. The centerline retardation increases with the Reynolds number, pointing once again towards a reduced effectiveness of the current drag reduction mechanism at higher Reynolds numbers.

Figure 9 shows the spectral decomposition of the net turbulent force as a function of the azimuthal wavelength at $Re_\tau = 720$. In the NWO cases, we observe a clear peak in the net turbulent force with the azimuthal wavelength $\lambda_s^+ \approx 100$, associated with the near-wall streak spacing, at the bottom of the buffer layer ($y^+ \approx 10$). The effect of wall oscillations, as was already seen in the streamwise spectra, is to diminish the magnitude of the net turbulent force as compared to the NWO case. We

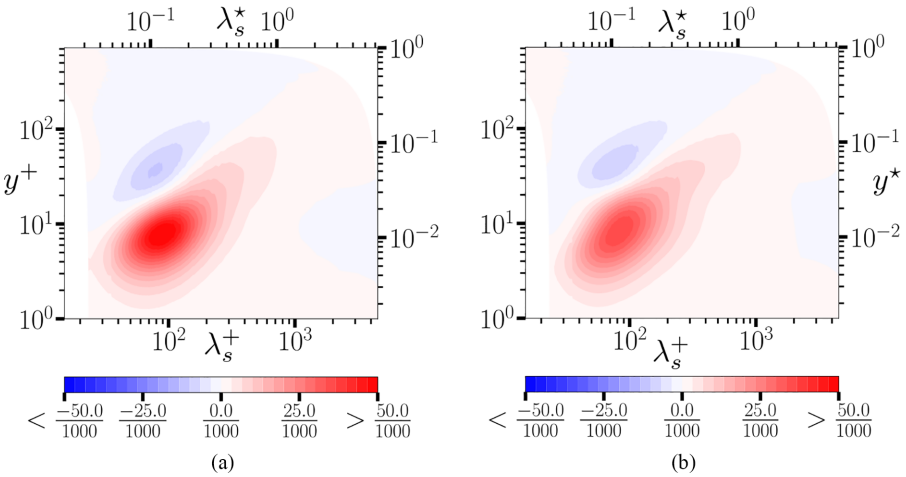

FIG. 9. Premultiplied azimuthal spectra of the net turbulent force, $F_{\text{turb}}^+(\lambda_s^+, y^+)$, for $Re_\tau = 720$. (a) NWO cases; (b) WO cases.

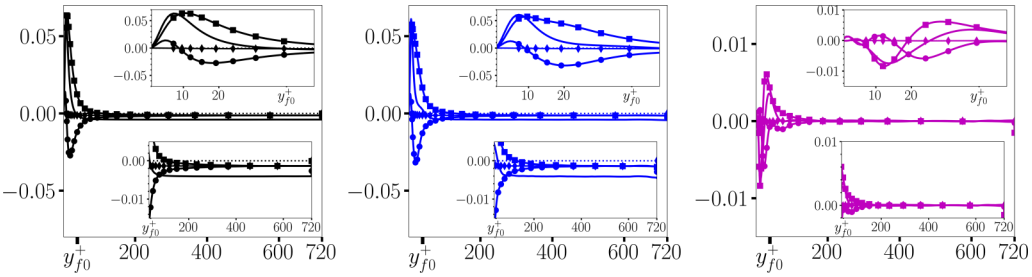

FIG. 10. Budget of the net turbulent force through the velocity-vorticity correlations at $\mathrm{Re}_\tau = 720$. From (a)–(c), NWO, WO, and Δ. The lines with no marks denote the total net turbulent force; lines with squares indicate the $-\langle u''^+_\theta \omega''^+_r \rangle$ term; lines with circles indicate the $\langle u''^+_r \omega''^+_\theta \rangle$ term; and the lines with diamonds indicate the $-\langle u''^+_x u''^+_r \rangle / r^+$ term. The top inset in each panel plots a zoom-in of the region of acceleration, $y^+ < y^+_{f0}$, while the bottom inset shows a zoom-in of the region of deceleration, $y^+ > y^+_{f0}$. The bottom axis in each panel also marks a location of y^+_{f0}. y^+_{f0} is taken from the NWO case. Dotted horizontal lines indicate the zero value.

observe that the reduction in the net turbulent force comes from the intermediate to large azimuthal scales of motion in the buffer layer ($\lambda^+_s > 100$), whose acceleration is retarded as a result of wall oscillations. The suppression of the net turbulent force in large streamwise and azimuthal scales due to wall oscillations is consistent with the hypothesis that wall oscillations inhibit the growth of the hairpin packets. The lack of growth in the large-scale structures forming the packets prevents formation of the low-momentum zones [62], which leads to a higher bulk flow rate in the WO cases.

The budget of the net turbulent force describes the contribution of the velocity-vorticity correlations to the turbulent force [74]. In cylindrical coordinates, such a decomposition applied to Eq. (12) can be shown to be

$$F_{\mathrm{turb}}(r)^+ = -\langle u''^+_\theta \omega''^+_r \rangle + \langle u''^+_r \omega''^+_\theta \rangle - \frac{\langle u''^+_x u''^+_r \rangle}{r^+}. \tag{17}$$

The first term on the right-hand side, $-\langle u''^+_\theta \omega''^+_r \rangle$, is the vortex stretching term [75,76]; the second term, $\langle u''^+_r \omega''^+_\theta \rangle$, is referred to as the advective vorticity transport; and the last term, $-\langle u''^+_x u''^+_r \rangle / r^+$, arises due to a cylindrical geometry of the problem. This allows for a physical interpretation of the effects causing the reduction in the net turbulent force.

Figure 10 shows the decomposition of the net turbulent force into its corresponding velocity-vorticity components at $\mathrm{Re}_\tau = 720$. It can be seen that the vortex stretching term, $-\langle u''^+_\theta \omega''^+_r \rangle$ [75,76], is the primary contributor to the flow acceleration (positive F^+_{turb}) in both NWO and WO flows. This term, however, is markedly reduced in the WO as compared to the NWO flows in the region of $y^+ < 20$, promoting reduction of the near-wall velocity gradient, while it is increased in the buffer, logarithmic, and wake regions with wall oscillation. It was found that the amount of reduction in the vortex stretching between WO and NWO cases diminishes with the Reynolds number (not displayed here for brevity).

The second budget term, $\langle u''^+_r \omega''^+_\theta \rangle$, the advective vorticity transport, has a smaller effect on the net turbulent force as compared to the vortex stretching term, and in fact mostly acts to decelerate the flow everywhere above $y^+ > 10$. Its contribution to a difference between the NWO and WO cases is also smaller as compared to the vortex stretching term, especially throughout the buffer layer. However, this effect of decelerating the flow is beneficial to drag reduction below y_{f0}. This is consistent with the drag reduction mechanism proposed by Choi and Clayton [65], who postulated that the streamwise vorticity gets reoriented along the spanwise direction as a result of the Stokes layer. This, in turn, creates positive spanwise vorticity in the near-wall region that acts to reduce velocity gradient by decelerating the mean flow near the wall. It is interesting to note the overall

effect of the pipe flow geometry (the third budget term, $-\langle u_x''^+ u_r''^+ \rangle / r^+$) to diminish F^+_{turb} and thus to decelerate the mean flow at all wall-normal locations. Its value is, however, significantly smaller than that of the other two terms and it reduces with the Reynolds number (not displayed here for brevity).

3. Contribution to bulk mean velocity

The Fukagata-Iwamoto-Kasagi (FIK) identity relates the wall shear stress to a componentwise contribution of different dynamical effects in a turbulent flow [77]. To assess the effect on drag reduction in the current setup, where the wall shear stress is fixed but the volumetric flow rate is allowed to vary, it is more appropriate to express the FIK identity in terms of the bulk mean velocity [78,79]. Such an expression for the bulk mean velocity was derived for the nonoscillated pipe flow as [77–79]

$$U^+_{\text{bulk}} = \frac{\text{Re}_\tau}{4} - \text{Re}_\tau \int_0^1 \langle u_x'^+ u_r'^+ \rangle r^{\star 2} dr^\star, \tag{18}$$

where $u_i' = u_i - \langle u_i \rangle$ is a standard (Reynolds) turbulent fluctuation, and $r^\star = r/R$ is a radial coordinate scaled with the outer units. There are two issues that arise with wall oscillation: (1) the wall velocity boundary conditions are no longer zero, and (2) the fluctuating Reynolds stresses $\langle u_x'^+ u_r'^+ \rangle = \langle u_x^{\phi+} u_r^{\phi+} \rangle + \langle u_x''^+ u_r''^+ \rangle$ now contain a phase-dependent component, $\langle u_x^{\phi+} u_r^{\phi+} \rangle$, and an uncorrelated turbulent fluctuating component, $\langle u_x''^+ u_r''^+ \rangle$, as per a triple decomposition with a temporally periodic mean flow [52] [see Eq. (8)]. It is shown in Ref. [48] that (1) nonzero azimuthal wall velocity does not alter expression (18), and (2) the contribution of a phase-dependent component, $\langle u_x^{\phi+} u_r^{\phi+} \rangle$, to the Reynolds stress is negligible. The FIK identity for the wall-oscillated pipe flows with a triple decomposition thus reads

$$U^+_{\text{bulk}} = \frac{\text{Re}_\tau}{4} - \text{Re}_\tau \int_0^1 \langle u_x''^+ u_r''^+ \rangle r^{\star 2} dr^\star. \tag{19}$$

The first term in Eq. (19) corresponds to the laminar contribution to the bulk mean velocity (i.e., a contribution from a corresponding parabolic flow profile which was to develop under the same mean pressure gradient in a laminar flow), and the second term corresponds to the turbulent contribution. Since laminar contribution scaled with Re_τ is identical between the NWO and WO cases, we turn our attention to the turbulent contribution. We can represent a turbulent contribution as a limiting value of the cumulative distribution function evaluated at the pipe centerline $r^\star = 0$ ($y^\star = 1$) as

$$U^{t,\text{cum}+}_{\text{bulk}}(y^\star) = -\text{Re}_\tau \int_{1-y^\star}^1 \langle u_x''^+ u_r''^+ \rangle r^{\star 2} dr^\star. \tag{20}$$

Figure 11 shows the cumulative turbulent contribution to the bulk mean velocity, as well as the spectra of the total turbulent contribution for the NWO and WO cases. From Fig. 11(b), one can observe that the major increase in the bulk mean velocity in a controlled flow as compared to the uncontrolled flow comes from the buffer and the logarithmic layer of the flow, with the peak around the top of the logarithmic layer, and the cumulative contribution decreasing in the outer layer. Figure 11(c) shows an increased contribution of large streamwise scales to the mean flow retardation by turbulence with increasing Reynolds number, with the effect of wall oscillation to suppress this retardation in the intermediate scales and to increase it in larger scales. Interestingly, an azimuthal spectrum presented in Fig. 11(d) shows a clear peak in $-U^{t+}_{\text{bulk}}$ at azimuthal scales around $\lambda_s^+ \approx 1000$ which increases with Re_τ. These scales, representative of the hairpin packet organization [28,80], contribute the most to the turbulent drag. An important result is that larger scales of motion in WO flows act to increase drag. This explains the decreased effectiveness of the wall oscillation mechanism (at least with the chosen oscillation parameters) at higher Reynolds numbers: there are stronger large-scale motions that develop at higher Re, and they are the ones which negatively effect drag reduction. Wall oscillation at the lowest Reynolds number, $\text{Re}_\tau = 170$, seems to be very effective at reducing drag in azimuthal scales corresponding to the individual

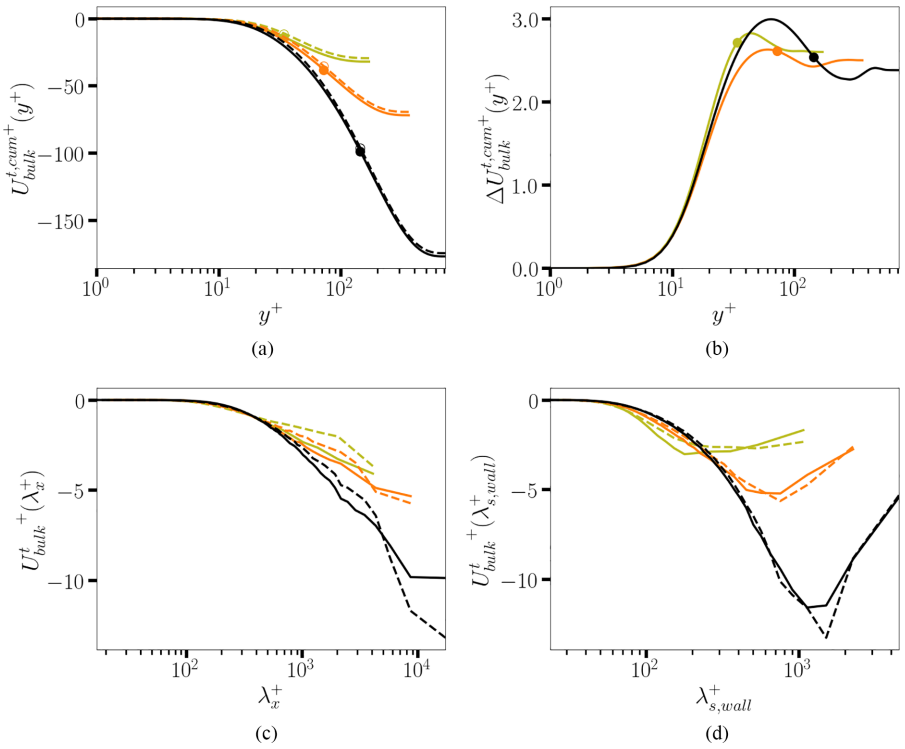

FIG. 11. Turbulent contribution to the bulk mean velocity. (a) Cumulative contribution, (b) change in contribution, (c) contribution by streamwise wavelength (λ_x^+), and (d) contribution by azimuthal wavelength ($\lambda^+_{s,\mathrm{wall}} = \lambda^+_s(R)$). Olive green is $\mathrm{Re}_\tau = 170$, orange is $\mathrm{Re}_\tau = 360$, and black is $\mathrm{Re}_\tau = 720$. [(a), (c), (d)] NWO, solid lines, and WO, dashed lines (except in (b) which shows a change). Circles in (a) and (b) indicate the location of the top of the logarithmic layer.

hairpins ($\lambda_s^+ \approx 100$–200), perhaps because the Reynolds number is too low to effectively form larger structures composed from the agglomeration of hairpins. Wall oscillation at the two higher Reynolds numbers, $\mathrm{Re}_\tau = 360$ and $\mathrm{Re}_\tau = 720$, favorably affects a larger range of azimuthal wavenumbers ($100 \leqslant \lambda_s^+ \leqslant 700$). Larger azimuthal scales, $\lambda_s^+ > 1000$, negatively contribute to drag reduction.

To characterize both the length scales and the wall-normal location of turbulent motions contributing to drag reduction, Fig. 12 plots the streamwise and azimuthal spectra of the cumulative turbulent contribution as a function of wall-normal coordinate at $\mathrm{Re}_\tau = 720$. It can be seen that the streamwise scales of motion with the wavelengths in the range $500 \leqslant \lambda_x^+ \leqslant 5000$ contribute to drag reduction (positive $\Delta\, U^{t,\mathrm{cum}^+}_{\mathrm{bulk}}(\lambda_x^+, y^+)$) all throughout the vertical extent of the pipe. It can also be noted that larger wavelengths, while still acting to cumulatively reduce drag (increase bulk flow rate) in the logarithmic layer, overtake and lead to a drag increase in the outer layer. This effect is absent at the lowest Reynolds number, $\mathrm{Re}_\tau = 170$, and is the strongest at the highest Reynolds number, $\mathrm{Re}_\tau = 720$ (not displayed here for brevity). For the azimuthal spectra, it is observed that the azimuthal length scales in the range $50 \leqslant \lambda_s^+ \leqslant 500$ act to reduce drag (increase bulk flow rate) while larger structures increase drag (reduce bulk flow rate), essentially independent of the wall-normal location. Interestingly, drag-reducing azimuthal scales organize themselves into a fractal-like pattern (red "fingers") visible in Fig. 12(b). A fractal-like pattern is consistent with the attached-eddy hypothesis of the near-wall turbulence [27,81] and a hierarchy of hairpin structures in a hairpin packet organization [28]; the fact that the drag-reducing motions adhere to this pattern suggests a link between the drag reduction mechanisms and a weakening of the hairpin packets.

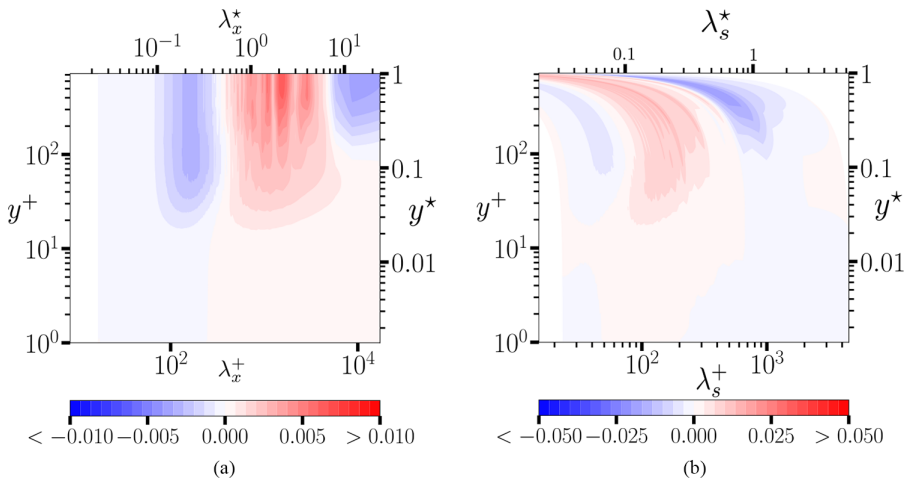

FIG. 12. Premultiplied change in the cumulative turbulent contribution spectra (normalized by the laminar contribution) as a function of wall-normal location and the wavelength at $\mathrm{Re}_\tau = 720$. (a) Streamwise spectrum, $\Delta\, 4U^{t,\mathrm{cum}+}_{\mathrm{bulk}}(\lambda_x^+, y^+)/\mathrm{Re}_\tau$; (b) azimuthal spectrum, $\Delta\, 4U^{t,\mathrm{cum}+}_{\mathrm{bulk}}(\lambda_s^+, y^+)/\mathrm{Re}_\tau$.

IV. CONCLUSIONS

The current study documents the results of direct numerical simulation of a turbulent pipe flow with and without transverse wall oscillation for three Reynolds numbers, $\mathrm{Re}_\tau = 170$, 360, and 720. It is found that wall oscillation results in an increase of a flow rate by almost 20% and, consequently, achieves a drag reduction of approximately 30% at the lowest Reynolds number; however, this effect decreases as the Reynolds number increases. Single-point statistics, log-law shift, one-dimensional spectra of streamwise kinetic energy, net turbulent force, and the turbulent contribution to the bulk mean velocity are analyzed to explain this effect.

It is found that the primary effect of wall oscillation is to reduce the energy and the net turbulent force in the intermediate to large streamwise and azimuthal scales of motion in the buffer layer of the flow. To the contrary, energy is increased in the large-scale structures in the logarithmic layer and the wake region. At the lowest Reynolds number, $\mathrm{Re}_\tau = 170$, the inner layer extends through ≈65% of the domain while it comprises ≈15% of the domain at $\mathrm{Re}_\tau = 720$. Since the overall attenuation of energetic structures is limited to the inner layer of the flow, a relatively larger portion of the flow occupied by the outer layer and, hence, by the unattenuated large-scale structures as the Reynolds number increases correlates with the reduced effectiveness of the wall oscillation in this parameter regime. This effect is well illustrated by Fig. 8, where low-pass filtered and high-pass filtered net turbulent force is plotted as a function of wall-normal coordinate. This figure shows that (a) most of the net turbulent force attenuation as a result of wall oscillation comes from the effect of the scales of $\lambda_x^+ > 1000$ (above the filter cutoff length) and (b) the reduction of the magnitude of the net turbulent force is confined to the buffer layer and the logarithmic layer of the flow. The reduction of the magnitude of the net turbulent force by wall oscillation results in a reduced flow acceleration in the near-wall layer from a corresponding laminar profile and an increased acceleration in the logarithmic layer as compared to the NWO cases, yielding a velocity profile which is less blunt and more "laminar-like." This is offset by an increase of the net turbulent force magnitude (promoting flow deceleration) above the logarithmic layer, leading to a lower ratio of the centerline velocity to the bulk velocity in WO cases, which is further lowered with Reynolds number. From the velocity-vorticity budget decomposition of the net turbulent force, it is observed that the reduction of the net turbulent force mostly comes from a suppression of the vortex stretching within the Stokes layer of the flow and its augmentation above the Stokes layer and below $y^+ \approx 100$. A reduced vortex stretching in

the Stokes layer inhibits a mutual induction of the hairpin legs which, in turn, reduces the liftup of the hairpins and formation of their necks, thus suppressing the hairpin autogeneration [82].

From superimposing the analysis of the streamwise and azimuthal spectra, together with the wall-normal location of the affected length scales, one can deduce the shape of the structures most affected by drag reduction. It can be seen that a significant energy reduction occurs at streamwise scales at and slightly above $\lambda_x^+ \approx 1000$ and at azimuthal scales at and slightly above $\lambda_s^+ \approx 100$, which corresponds to the scales of motion typically associated with the hairpin packets [28,80]. Since streaks and quasistreamwise vortices are closely related, wall oscillation presumably weakens the quasistreamwise near-wall vortices, thereby reducing their transport of streamwise momentum into the streaks. This is consistent with the observations of Yao *et al.* [18], who reported a suppression of Reynolds shear stresses at $\lambda_s^+ < 400$ in a turbulent channel flow with wall oscillation. This points towards a suppression of hairpin packets by wall oscillation being one of the main mechanisms of drag reduction in the "inner-scaled" actuation regime. It is hypothesized that the autogeneration mechanism of turbulence [69,82,83] is suppressed by the wall oscillation in the present pipe flow configuration, thus attenuating the formation and growth of the hairpin packets. Interestingly, the shorter streamwise scales of motion, $\lambda_x^+ < 500$, are amplified, which may be due to a breakdown of quasistreamwise vortices by wall oscillation that redistributes energy from larger into smaller scales and ultimately hinders the ability of near-wall structures to regenerate [15,65]. Large streamwise scales, $\lambda_x^+ > 5000$, and large azimuthal scales, $\lambda_s^+ > 1000$, are also found to be amplified by wall oscillation, both in the buffer layer and above.

A convincing evidence of the effect of different scales of motion on drag reduction comes from the spectral analysis of the FIK identity [77], specifically, of the turbulent contribution to the bulk mean velocity. To this end, Fig. 11 demonstrates a remarkable collapse of the difference in its spectra between the NWO and WO cases across all three Reynolds numbers, showing that the drag reduction is limited to the streamwise wavelengths of $\lambda_x^+ < 5000$ independent of the Reynolds number. The wavelengths with $\lambda_x^+ > 5000$, exerting increasingly larger dominance, especially in the outer layer, act to increase drag. This explains the observed reduction of effectiveness of wall oscillation as a drag reduction mechanism in pipe flows with the increase in Reynolds number in the considered parameter regime, which is optimized for controlling the near-wall cycle of turbulence [6,8,9,35]. Further studies are needed to establish whether the presented conclusions hold at larger Reynolds numbers and at different wall oscillation parameter regimes. Additionally, the current work suggests that even longer domain sizes might be required to properly capture the large scale and very large scales of motions in wall-oscillated flows as compared to the nonoscillated ones, due to a potential amplification of these scales by wall oscillation.

ACKNOWLEDGMENTS

This research was supported by the NSF CAREER Award No. CBET-1944568 and by the Ira A. Fulton Professorship endowment. The computational time has been provided by NSF ACCESS supercomputing resources.

The authors report no conflict of interest.

[1] M. Gad-el-Hak, Interactive control of turbulent boundary layers—a futuristic overview, AIAA J. **32**, 1753 (1994).

[2] M. R. Abbassi, W. J. Baars, N. Hutchins, and I. Marusic, Skin-friction drag reduction in a high-Reynolds-number turbulent boundary layer via real-time control of large-scale structures, Int. J. Heat Fluid Flow **67**, 30 (2017).

[3] M. Fingas, Review of the 2015 Alaska North Slope oil properties relevant to environmental assessment and prediction, Prince William Sound Regional Citizens' Advisory Council (PWSRCAC) report (2016).

[4] R. Wood, Reynolds number impact on commercial vehicle aerodynamics and performance, SAE Int. J. Commer. Veh. **8**, 590 (2015).
[5] M. A. Leschziner, Friction-drag reduction by transverse wall motion—a review, J. Mech. **36**, 649 (2020).
[6] W.-J. Jung, N. Mangiavacchi, and R. Akhavan, Suppression of turbulence in wall-bounded flows by high-frequency spanwise oscillations, Phys. Fluids A **4**, 1605 (1992).
[7] A. Baron and M. Quadrio, Turbulent drag reduction by spanwise wall oscillations, Appl. Sci. Res. **55**, 311 (1996).
[8] K.-S. Choi and M. Graham, Drag reduction of turbulent pipe flows by circular-wall oscillation, Phys. Fluids **10**, 7 (1998).
[9] M. Quadrio and P. Ricco, Critical assessment of turbulent drag reduction through spanwise wall oscillations, J. Fluid Mech. **521**, 251 (2004).
[10] P. Ricco, M. Skote, and M. A. Leschziner, A review of turbulent skin-friction drag reduction by near-wall transverse forcing, Prog. Aerosp. Sci. **123**, 100713 (2021).
[11] M. Quadrio, P. Ricco, and C. Viotti, Streamwise-travelling waves of spanwise wall velocity for turbulent drag reduction, J. Fluid Mech. **627**, 161 (2009).
[12] D. Gatti and M. Quadrio, Performance losses of drag-reducing spanwise forcing at moderate values of the Reynolds number, Phys. Fluids **25**, 125109 (2013).
[13] E. Hurst, Q. Yang, and Y. M. Chung, The effect of Reynolds number on turbulent drag reduction by streamwise travelling waves, J. Fluid Mech. **759**, 28 (2014).
[14] M.-X. Zhao, W.-X. Huang, and C.-X. Xu, Drag reduction in turbulent flow along a cylinder by circumferential oscillating Lorentz force, Phys. Fluids **31**, 095104 (2019).
[15] X. Liu, H. Zhu, Y. Bao, D. Zhou, and Z. Han, Turbulence suppression by streamwise-varying wall rotation in pipe flow, J. Fluid Mech. **951**, A35 (2022).
[16] E. Touber and M. A. Leschziner, Near-wall streak modification by spanwise oscillatory wall motion and drag-reduction mechanisms, J. Fluid Mech. **693**, 150 (2012).
[17] D. Gatti and M. Quadrio, Reynolds-number dependence of turbulent skin-friction drag reduction induced by spanwise forcing, J. Fluid Mech. **802**, 553 (2016).
[18] J. Yao, X. Chen, and F. Hussain, Reynolds number effect on drag control via spanwise wall oscillation in turbulent channel flows, Phys. Fluids **31**, 085108 (2019).
[19] I. Marusic, D. Chandran, A. Rouhi, M. K. Fu, D. Wine, B. Holloway, D. Chung, and A. J. Smits, An energy-efficient pathway to turbulent drag reduction, Nat. Commun. **12**, 5805 (2021).
[20] A. Rastegari and R. Akhavan, On drag reduction scaling and sustainability bounds of superhydrophobic surfaces in high Reynolds number turbulent flows, J. Fluid Mech. **864**, 327 (2019).
[21] G. Gómez-de-Segura and R. García-Mayoral, Turbulent drag reduction by anisotropic permeable substrates–analysis and direct numerical simulations, J. Fluid Mech. **875**, 124 (2019).
[22] L. Agostini and M. Leschziner, Statistical analysis of outer large-scale/inner-layer interactions in channel flow subjected to oscillatory drag-reducing wall motion using a multiple-variable joint-probability-density function methodology, J. Fluid Mech. **923**, A25 (2021).
[23] C. Di Nucci and R. Absi, Comparison of mean properties of turbulent pipe and channel flows at low-to-moderate Reynolds numbers, Fluids **8**, 97 (2023).
[24] J. P. Monty, N. Hutchins, H. C. H. Ng, I. Marusic, and M. S. Chong, A comparison of turbulent pipe, channel and boundary layer flows, J. Fluid Mech. **632**, 431 (2009).
[25] A. J. Smits, B. J. McKeon, and I. Marusic, High-Reynolds number wall turbulence, Annu. Rev. Fluid Mech. **43**, 353 (2011).
[26] D. J. Coxe, Y. T. Peet, and R. J. Adrian, On Stokes' second problem solutions in cylindrical and Cartesian domains, Phys. Fluids **34**, 103615 (2022).
[27] A. Townsend, The structure of the turbulent boundary layer, in *Mathematical Proceedings of the Cambridge Philosophical Society* (Cambridge University Press, Cambridge, UK, 1951), Vol. 47, pp. 375–395.
[28] R. J. Adrian, Hairpin vortex organization in wall turbulence, Phys. Fluids **19**, 041301 (2007).
[29] J. Jiménez, Coherent structures in wall-bounded turbulence, J. Fluid Mech. **842**, P1 (2018).
[30] S. Nakashima, K. Fukagata, and M. Luhar, Assessment of suboptimal control for turbulent skin friction reduction via resolvent analysis, J. Fluid Mech. **828**, 496 (2017).

[31] S. S. Toedtli, M. Luhar, and B. J. McKeon, Predicting the response of turbulent channel flow to varying-phase opposition control: Resolvent analysis as a tool for flow control design, Phys. Rev. Fluids **4**, 073905 (2019).
[32] S. Pirozzoli, J. Romero, M. Fatica, R. Verzicco, and P. Orlandi, One-point statistics for turbulent pipe flow up to $\mathrm{Re}_\tau \approx 6000$, J. Fluid Mech. **926**, A28 (2021).
[33] J. Yao, S. Rezaeiravesh, P. Schlatter, and F. Hussain, Direct numerical simulations of turbulent pipe flow up to $\mathrm{Re}_\tau \approx 5200$, J. Fluid Mech. **956**, A18 (2023).
[34] A. Rouhi, M. K. Fu, D. Chandran, A. Zampiron, A. J. Smits, and I. Marusic, Turbulent drag reduction by spanwise wall forcing. 1. Large-eddy simulations, J. Fluid Mech. **968**, A6 (2023).
[35] D. Chandran, A. Zampiron, A. Rouhi, M. K. Fu, D. Wine, B. Holloway, A. J. Smits, and I. Marusic, Turbulent drag reduction by spanwise wall forcing. Part 2. High-Reynolds-number experiments, J. Fluid Mech. **968**, A7 (2023).
[36] N. Nikitin, On the mechanism of turbulence suppression by spanwise surface oscillations, Fluid Dyn. **35**, 185 (2000).
[37] M. Quadrio and S. Sibilla, Numerical simulation of turbulent flow in a pipe oscillating around its axis, J. Fluid Mech. **424**, 217 (2000).
[38] J.-I. Choi, C.-X. Xu, and H. J. Sung, Drag reduction by spanwise wall oscillation in wall-bounded turbulent flows, AIAA J. **40**, 842 (2002).
[39] A. Duggleby, K. S. Ball, M. R. Paul, and P. F. Fischer, Dynamical eigenfunction decomposition of turbulent pipe flow, J. Turbul. **8**, N43 (2007).
[40] F. Auteri, A. Baron, M. Belan, G. Campanardi, and M. Quadrio, Experimental assessment of drag reduction by traveling waves in a turbulent pipe flow, Phys. Fluids **22**, 115103 (2010).
[41] L. Ding, L. Sabidussi, B. C. Holloway, M. Hultmark, and A. J. Smits, Acceleration is the key to drag reduction in turbulent flow, arXiv:2312.12591.
[42] G. K. El Khoury, P. Schlatter, A. Noorani, P. F. Fischer, G. Brethouwer, and A. V. Johansson, Direct numerical simulation of turbulent pipe flow at moderately high Reynolds numbers, Flow, Turbul. Combust. **91**, 475 (2013).
[43] K.-S. Choi, J.-R. DeBisschop, and B. R. Clayton, Turbulent boundary-layer control by means of spanwise-wall oscillation, AIAA J. **36**, 1157 (1998).
[44] R. L. Panton, *Incompressible Flow* (Wiley, New York, 1984).
[45] M. O. Deville, P. F. Fischer, and E. H. Mund, *High-Order Methods for Incompressible Fluid Flow* (Cambridge University Press, Cambridge, UK, 2002).
[46] P. Fischer, J. Lottes, S. Kerkemeier, O. Marin, K. Heisey, A. Obabko, E. Merzari, and Y. Peet, Nek5000: User's manual, ANL Report No. ANL/MCS-TM-351 (2015).
[47] A. Duggleby, K. Ball, and M. R. Paul, The effect of spanwise wall oscillation on turbulent pipe flow structures resulting in drag reduction, Phys. Fluids **19**, 125107 (2007).
[48] D. Coxe, Y. Peet, and R. Adrian, Reynolds number effect on drag reduction in pipe flows by a transverse wall oscillation, arXiv:2312.03232.
[49] G. Nikuradse, Yearbook 1932 of the Deutsche Versuchsanstalt fr Luftfahrt. Edited by Dr.-Ing. Wilh Hoff. Berlin and Munich, 1932. (R. Oldenburg, publisher.) Price R.M. 35, J. Roy. Aeronaut. Soc. **36**, 1050 (1932).
[50] H. Schlichting and K. Gersten, *Boundary-Layer Theory* (Springer, Berlin, 2016).
[51] K. Hillewaert, C. C. de Wiart, and J.-S. Cagnone, WS2 LES of the plane channel at Ret = 550, in *Proceedings of HiOCFD5 5th International Workshop on High-Order CFD Methods* (Cenaero, Gosselies, Belgium, 2017).
[52] A. K. M. F. Hussain and W. C. Reynolds, The mechanics of an organized wave in turbulent shear flow, J. Fluid Mech. **41**, 241 (1970).
[53] H. Blasius, Das aehnlichkeitsgesetz bei reibungsvorgängen in flüssigkeiten, in *Mitteilungen über Forschungsarbeiten auf dem Gebiete des Ingenieurwesens: Insbesondere aus den Laboratorien der technischen Hochschulen* (Springer, Berlin, 1913), pp. 1–41.
[54] L. F. Moody, Friction factors for pipe flow, Trans. ASME **66**, 671 (1944).
[55] M. V. Zagarola and A. J. Smits, Mean-flow scaling of turbulent pipe flow, J. Fluid Mech. **373**, 33 (1998).

[56] P. Ricco and M. Quadrio, Wall-oscillation conditions for drag reduction in turbulent channel flow, Int. J. Heat Fluid Flow **29**, 891 (2008).
[57] R. Akhavan, R. Kamm, and A. Shapiro, An investigation of transition to turbulence in bounded oscillatory Stokes flows. Part 1. Experiments, J. Fluid Mech. **225**, 395 (1991).
[58] K.-S. Choi, Near-wall structure of turbulent boundary layer with spanwise-wall oscillation, Phys. Fluids **14**, 2530 (2002).
[59] J. H. Lee, H. J. Sung, and R. J. Adrian, Space–time formation of very-large-scale motions in turbulent pipe flow, J. Fluid Mech. **881**, 1010 (2019).
[60] R. J. Adrian, S. Balachandar, and Z. Lin, Spanwise growth of vortex structure in wall turbulence, KSME Int. J. **15**, 1741 (2001).
[61] P. Schlatter, Q. Li, R. Örlü, F. Hussain, and D. S. Henningson, On the near-wall vortical structures at moderate Reynolds numbers, Eur. J. Mech. B Fluids **48**, 75 (2014).
[62] C. M. de Silva, N. Hutchins, and I. Marusic, Uniform momentum zones in turbulent boundary layers, J. Fluid Mech. **786**, 309 (2016).
[63] Y. Motoori and S. Goto, Hairpin vortices in the largest scale of turbulent boundary layers, Int. J. Heat Fluid Flow **86**, 108658 (2020).
[64] J. Jiménez, The streaks of wall-bounded turbulence need not be long, J. Fluid Mech. **945**, R3 (2022).
[65] K.-S. Choi and B. R. Clayton, The mechanism of turbulent drag reduction with wall oscillation, Int. J. Heat Fluid Flow **22**, 1 (2001).
[66] C. M. White, V. S. R. Somandepalli, and M. G. Mungal, The turbulence structure of drag-reduced boundary layer flow, Exp. Fluids **36**, 62 (2004).
[67] K. Kim, C.-F. Li, R. Sureshkumar, S. Balachandar, and R. J. Adrian, Effects of polymer stresses on Eddy structures in drag-reduced turbulent channel flow, J. Fluid Mech. **584**, 281 (2007).
[68] Z.-L Zhang, M.-M. Zhang, C. Cai, and Y. Cheng, Characteristics of large-and small-scale structures in the turbulent boundary layer over a drag-reducing riblet surface, Proc. Inst. Mech. Eng. Part C: J. Mech. Eng. Sci. **234**, 796 (2020).
[69] K. Kim, R. J. Adrian, S. Balachandar, and R. Sureshkumar, Dynamics of hairpin vortices and polymer-induced turbulent drag reduction, Phys. Rev. Lett. **100**, 134504 (2008).
[70] M. Guala, S. Hommema, and R. Adrian, Large-scale and very-large-scale motions in turbulent pipe flow, J. Fluid Mech. **554**, 521 (2006).
[71] D. Coxe, Y. Peet, and R. Adrian, Convection velocity in drag-reduced oscillating pipe flow, in *Proceedings of the 12th International Symposium on Turbulence and Shear Flow Phenomena* (Elsevier, Amsterdam, 2022).
[72] B. Balakumar and R. Adrian, Large- and very-large-scale motions in channel and boundary-layer flows, Philos. Trans. R. Soc. A **365**, 665 (2007).
[73] X. Wu, J. Baltzer, and R. Adrian, Direct numerical simulation of a 30R long turbulent pipe flow at R+= 685: Large-and very large-scale motions, J. Fluid Mech. **698**, 235 (2012).
[74] J. Klewicki, Velocity–vorticity correlations related to the gradients of the Reynolds stresses in parallel turbulent wall flows, Phys. Fluids **1**, 1285 (1989).
[75] M. Yoon, J. Ahn, J. Hwang, and H. J. Sung, Contribution of velocity-vorticity correlations to the frictional drag in wall-bounded turbulent flows, Phys. Fluids **28**, 081702 (2016).
[76] Q. Chen, R. J. Adrian, Q. Zhong, D. Li, and X. Wang, Experimental study on the role of spanwise vorticity and vortex filaments in the outer region of open-channel flow, J. Hydraul. Res. **52**, 476 (2014).
[77] K. Fukagata, K. Iwamoto, and N. Kasagi, Contribution of Reynolds stress distribution to the skin friction in wall-bounded flows, Phys. Fluids **14**, L73 (2002).
[78] I. Marusic, D. D. Joseph, and K. Mahesh, Laminar and turbulent comparisons for channel flow and flow control, J. Fluid Mech. **570**, 467 (2007).
[79] A. Yakeno, Y. Hasegawa, and N. Kasagi, Modification of quasi-streamwise vortical structure in a drag-reduced turbulent channel flow with spanwise wall oscillation, Phys. Fluids **26**, 085109 (2014).
[80] R. J. Adrian, C. D. Meinhart, and C. D. Tomkins, Vortex organization in the outer region of the turbulent boundary layer, J. Fluid Mech. **422**, 1 (2000).

[81] Y. Hwang, Statistical structure of self-sustaining attached eddies in turbulent channel flow, J. Fluid Mech. **767**, 254 (2015).

[82] J. Zhou, R. J. Adrian, S. Balachandar, and T. Kendall, Mechanisms for generating coherent packets of hairpin vortices in channel flow, J. Fluid Mech. **387**, 353 (1999).

[83] K. U. Kempaiah, F. Scarano, G. E. Elsinga, B. W. Van Oudheusden, and L. Bermel, 3-dimensional particle image velocimetry based evaluation of turbulent skin-friction reduction by spanwise wall oscillation, Phys. Fluids **32**, 085111 (2020).